

## Wavefield reconstruction by interpolating significantly decimated boundaries

Pengliang Yang<sup>1</sup>, Romain Brossier<sup>1</sup>, and Jean Virieux<sup>1</sup>

### ABSTRACT

Many practical seismic applications such as reverse time migration (RTM) and full-waveform inversion (FWI) are usually computation and memory intensive. To perform crosscorrelation in RTM or build the gradient for FWI, it is mandatory to access the forward and adjoint wavefields simultaneously. To do this, there are three methods: One is to read the stored forward wavefield from the disk, the second is using the final snapshot and the stored boundaries via reverse propagation, and the third is remodeling using checkpointing from stored state to another state. Among these techniques, wavefield reconstruction by reverse propagation appears to be a quite straightforward approach; however, it suffers a stringent memory bottleneck for 3D large-scale imaging applications. The Courant-Friedrichs-Lewy (CFL) condition is a fundamental criterion to determine temporal sampling to achieve stable wavefield extrapolation. The injection of the boundary sequence in time is essentially

determined by Nyquist sampling principle, rather than the time interval given by CFL, which is much smaller than the Nyquist requirement. Based on this recognition, we have developed three boundary interpolation techniques, such as the discrete Fourier transform (DFT) interpolation, Kaiser windowed sinc interpolation, and Lagrange polynomial interpolation, for wavefield reconstruction to move from CFL to the Nyquist limit. Wavefield reconstruction via DFT interpolation can be implemented by folding and unfolding steps in the forward simulation and backward reconstruction on the fly. Compared with the DFT interpolation, the wavefield reconstruction methods using Kaiser windowed sinc interpolation and Lagrange polynomial interpolation have better efficiency while remaining a competitive accuracy. These methods allow us to dramatically decimate the boundary without significant loss of information, and they nicely reconstruct the boundary elements in between the samples, making the in-core memory saving of the boundaries feasible in 3D large-scale imaging applications.

### INTRODUCTION

Many practical seismic applications such as reverse time migration (RTM) and full-waveform inversion (FWI) are usually computation and memory intensive due to the small discretization interval and a much larger number of simulation time steps. To perform crosscorrelation in RTM or build the gradient for FWI in the time domain, it is mandatory to access the forward and adjoint wavefields simultaneously. There are several candidate strategies: (1) The most intuitive strategy is to save the source wavefield in core memory and on disk when forward modeling, and access it when computing the gradient, which is highly not recommended because the I/O cost via accessing the data on disk is generally more time consuming than computation; (2) a very efficient scheme is wavefield reconstruction

based on the saved boundaries and the final wavefield snapshot, which allows us to calculate the adjoint wavefield while computing the forward wavefield backward on the fly (Clapp, 2008; Dussaud et al., 2008; Brossier et al., 2014) — note that an alternative using the random boundary condition (Clapp et al., 2009; Shen and Clapp, 2015) avoids the boundary storing burden, which is still based on the idea of wavefield reconstruction and is strongly data dependent because the random layers have to be designed according to the goal of application (in migration to decay the low frequencies while in waveform inversion to tune the frequency parameter to decay the high frequencies); and (3) another option is the optimal checkpointing technique (Griewank, 1992; Griewank and Walther, 2000; Symes, 2007; Anderson et al., 2012) to do remodeling from one state to another state, which is considered to be much better than the first

Manuscript received by the Editor 22 December 2015; revised manuscript received 28 February 2016; published online 11 July 2016.

<sup>1</sup>University Grenoble Alpes, ISTerre, Grenoble, France. E-mail: pengliang.yang@univ-grenoble-alpes.fr; romain.brossier@univ-grenoble-alpes.fr; jean.virieux@univ-grenoble-alpes.fr.

© 2016 Society of Exploration Geophysicists. All rights reserved.

strategy; however, it involves more computation and memory resources compared with the second strategy.

To the best of our knowledge, the second scheme, namely, the initial value source wavefield reconstruction approach, seems to be the most appealing method for real applications. A perfect reconstruction can be achieved for nondissipative media via recomputing the forward wavefield backward using final snapshot and boundary condition. The boundaries saved at each time step during the forward simulation are usually injected into the computing box at every reverse propagation step. In the forward simulation and backward computation of the wave propagation, the Courant-Friedrichs-Lewy (CFL) condition is an extremely important criterion to determine the temporal sampling to achieve stable wavefield extrapolation. In 3D cases, the required amount of memory determined by CFL for wavefield reconstruction using the boundaries can be too large to be stored by the in-core memory, which is a major drawback to limit the use of this technique for 3D production scale applications.

The time interval given by CFL condition is, however, much smaller than the requirement of Nyquist sampling theorem for an accurate wavefield representation. Although the CFL is a necessary condition for stability when solving partial differential equations with numerical methods such as finite difference (FD), the injection of the boundary sequence in time is however determined by Nyquist sampling principle, rather than the CFL pitfall. Based on this recognition, in this paper we present three boundary interpolation techniques, such as discrete Fourier transform (DFT) interpolation, Kaiser windowed sinc interpolation, and Lagrange polynomial interpolation, for wavefield reconstruction to move from CFL constraint to the Nyquist limit. These techniques allow us to significantly decimate the boundary without much loss of information, and accurately reconstruct the boundary elements in between the samples, making the in-core memory saving of the boundaries practically feasible in 3D large-scale imaging applications.

The structure of the paper is organized as follows. First, the memory bound is identified as a practical bottleneck in 3D large-scale imaging and inversion problems to illustrate the significance of the Nyquist sampling to break through the boundary bottleneck determined by CFL. Then, we present the implementation of the three interpolation algorithms in wavefield reconstruction based on the acquired boundaries. Using a realistic 1D synthetic seismic trace, we investigate the accuracy of the three interpolation methods to obtain some empirical knowledge about their interpolation performance on seismic signal before application to the wavefield reconstruction. Then, we demonstrate validity of the proposed interpolation-based wavefield reconstruction approaches using 2D Marmousi model, by reverse reconstructing the forward wavefield based on the significantly downsampled boundaries. Finally, we analyze the computational complexity and the significance of memory saving in 3D context, to show that the proposed methods are able to reduce the boundary saving burden at least an order of magnitude in realistic models, therefore enabling efficient computation of 3D imaging problem (such as RTM and FWI) of moderate size using in-core memory saving of boundaries.

## WAVEFIELD RECONSTRUCTION FOR CROSSCORRELATION IN RTM AND FWI

The first-order system of wave motion reads in isotropic acoustic media

$$\begin{cases} \rho \partial_t \mathbf{v} = \nabla p + f_v \\ \partial_t p = \kappa \nabla \cdot \mathbf{v} + f_p \end{cases} \quad \text{or} \quad \underbrace{\begin{bmatrix} \rho I_3 & 0 \\ 0 & 1/\kappa \end{bmatrix}}_{N^{-1}(\mathbf{m})} \underbrace{\partial_t}_{\mathbf{u}} \underbrace{\begin{bmatrix} \mathbf{v} \\ p \end{bmatrix}}_{\mathbf{u}} = \underbrace{\begin{bmatrix} 0 & \nabla \\ \nabla \cdot & 0 \end{bmatrix}}_{H(\nabla)} \underbrace{\begin{bmatrix} \mathbf{v} \\ p \end{bmatrix}}_{\mathbf{u}} + \underbrace{\begin{bmatrix} f_v \\ f_p/\kappa \end{bmatrix}}_{\mathbf{s}}, \quad (1)$$

where  $\nabla \cdot$  is associated with the divergence of particle velocity vector; the stress and the particle velocities are, respectively, denoted as  $p$  and  $\mathbf{v} = (v_x, v_y, v_z)$  that are functions of time and space, i.e.,  $p = p(\mathbf{x}, t)$  and  $\mathbf{v} = \mathbf{v}(\mathbf{x}, t)$ . The function  $f_p$  and  $f_v$  are the corresponding sources,  $\rho$  stands for the density, and  $\kappa$  is the bulk modulus,  $\kappa = \rho v^2$ .

The principle of RTM imaging can be understood as the cross-correlation of two wavefields at the same time level, one computed by the forward time recursion and the other computed by the backward time stepping (Symes, 2007). The crosscorrelation imaging condition for RTM is specified by

$$I(\mathbf{x}) = \int_0^T dt p_s(\mathbf{x}, t) p_r(\mathbf{x}, t), \quad (2)$$

where  $I(\mathbf{x})$  is the migrated image at the point  $\mathbf{x}$ ; and  $p_s(\mathbf{x}, t)$  and  $p_r(\mathbf{x}, t)$  are the source and receiver wavefield, respectively. FWI is a powerful technique to retrieve quantitative high-resolution model parameters  $\mathbf{m} = (\rho, \kappa)$  of the subsurface by iteratively minimizing a misfit functional  $C(\mathbf{m})$  defined by the distance between the observed data and the synthetic seismograms (Virieux and Operto, 2009). The time-domain gradient expression in FWI can be written as (Brossier et al., 2014)

$$\nabla C(\mathbf{m}) = \int_0^T dt \lambda^\dagger(\mathbf{x}, t) \frac{\partial N^{-1}(\mathbf{m})}{\partial \mathbf{m}} \partial_t \mathbf{u}(\mathbf{x}, t), \quad (3)$$

where  $\lambda(\mathbf{x}, t)$  are the so-called adjoint wavefields.

As shown in equations 2 and 3 and illustrated in Figure 1, it is mandatory to access the forward wavefield and the receiver wavefield or adjoint wavefield simultaneously to perform crosscorrelation in RTM or build the gradient for FWI. This can be achieved either by reading the incident wavefield stored on disk or recovering the incident wavefield through reverse propagation using the final snapshot and saved boundaries (Clapp, 2008; Dussaud et al., 2008; Brossier et al., 2014), or through repeated remodeling via checkpointing technology (Griewank, 1992; Griewank and Walther, 2000; Symes, 2007; Anderson et al., 2012). The time devoted to slow disk memory access and comparatively large computation easily shifts the comparison in favor of wavefield reconstruction technique if there is enough in-core memory to store the large volume of boundary elements, which is usually a bottleneck in most state-of-the-art machines.

## WAVEFIELD RECONSTRUCTION FROM SIGNIFICANTLY DECIMATED BOUNDARIES

### Feasibility of significant downsampling on boundary: From CFL to Nyquist

CFL condition is a fundamental requirement for stable forward modeling in time

$$\frac{\Delta t v_{\max}}{\Delta x} \sum_{i=1}^J |a_i| \leq \frac{1}{\sqrt{D}} \Rightarrow \Delta t \leq \frac{\Delta x}{v_{\max}} \frac{1}{\sqrt{D} \sum_{i=1}^J |a_i|}, \quad (4)$$

where  $a_i$  is the coefficient of the staggered grid FD of order  $2J$  (Virieux, 1986; Fornberg, 1988),  $\Delta t$  and  $\Delta x$  are the temporal and spatial interval after discretization,  $v_{\max}$  is the maximum velocity, and  $D$  is the number of dimensions. Typically, we consider a 3D case with fourth-order spatial FD discretization: five grid points per minimum wavelength are enough to achieve accurate wave propagation for fourth-order FD discretization. That is,

$$\begin{aligned} \Delta x &= \frac{\lambda_{\min}}{5} = \frac{v_{\min}}{5f_{\max}} \Rightarrow \Delta t \leq \frac{0.49487\Delta x}{v_{\max}} \\ &\approx \frac{0.1}{f_{\max}} \frac{v_{\min}}{v_{\max}} < \frac{0.1}{f_{\max}} (v_{\min} \leq v_{\max}), \end{aligned} \quad (5)$$

in which  $f_{\max}$  and  $v_{\min}$  are the maximum frequency of the signal and minimum velocity of the media, respectively.

The Nyquist sampling theorem states that a signal can be perfectly reconstructed as long as the sampling frequency is no less than twice of the maximum frequency of the raw signal:

$$f_s \geq 2f_{\max} \Rightarrow \Delta t \leq \frac{0.5}{f_{\max}}. \quad (6)$$

It implies that the boundary saving process could be loosely downsampled with a ratio  $r$  without any information loss. Here, the ratio is

$$r_{3D} = \left(\frac{0.5}{f_{\max}}\right) / \left(\frac{0.1}{f_{\max}} \frac{v_{\min}}{v_{\max}}\right) = \frac{5v_{\max}}{v_{\min}}, \quad r_{2D} = \sqrt{\frac{2}{3}} r_{3D}. \quad (7)$$

All the boundaries are allowed to be reconstructed perfectly using the subsampled series, based on the Nyquist sampling principle. Compared with the Nyquist criterion 6, the CFL constraint 5 is too restrictive. There is at least five times of possible improvement for CFL to reach Nyquist bound in 3D acoustic medium. As a rule of thumb, in practical applications  $v_{\max}/v_{\min} \geq 3$  for acoustic media, whereas going up to 10 can be found in elastic media between the slowest S-wave and the fastest P-wave. In principle, we are able to reduce at least 15 times of boundary storing burden for acoustic media, whereas reducing up to 50 in elastic media. It is important to point out that significant downsampling is also valid in the framework of the second-order wave equation system, although the above analysis is done within the framework of the first-order wave equation system.

### Wavefield reconstruction via DFT interpolation

The Nyquist theorem states that Fourier transform allows perfect reconstruction of the bandlimited signal. A signal  $s(t)$  and its Fourier transform  $\tilde{s}(\omega)$  offer the flexibility of time and frequency scaling with a ratio  $r$

$$s(rt) \overset{\mathbb{F}}{\longleftrightarrow} \frac{1}{r} \tilde{s}\left(\frac{\omega}{r}\right), \quad \text{and} \quad \frac{1}{r} s\left(\frac{t}{r}\right) \overset{\mathbb{F}}{\longleftrightarrow} \tilde{s}(r\omega). \quad (8)$$

This implies that if a signal is expanded in one domain it is compressed in the dual domain. This is also called the uncertainty principle of Fourier analysis, which implies that if a continuous signal is subsampled with a factor  $r$ , the spectrum will be compressed  $r$  times, while the amplitude is proportionally changed with a ratio of  $r$ . Inspired by this fact, we propose a wavefield reconstruction method based on DFT interpolation technique. The implementation (see Appendix A) is applying a boxcar window on the frequency spectrum of the time series. Therefore, DFT interpolation can also be referred to as sinc interpolation because application of a frequency domain box is equivalent to convolving a time-domain sinc function with an infinite number of points (see Appendix B for more details). Instead of storing the elements in the boundary area, we store the Fourier coefficients for different frequencies computed with DFT, by multiplying a complex exponential factor on the fly during forward modeling, and summing over all frequencies with the conjugate of the exponential factor using inverse DFT in the backward reconstruction. The idea of computing DFT on the fly is a good prescription of the memory consumption issue in waveform inversion, which can also be found in the literature (Sirgue et al., 2007; Brossier et al., 2014).

Let us denote the state variables as  $u(\mathbf{x}, t) \in \{\mathbf{v}(\mathbf{x}, t), p(\mathbf{x}, t)\}$ ,  $\mathbf{x} \in \Omega_b$  in which  $\Omega_b$  specifies the boundary area where we can store in core memory. Keep in mind that the whole time history  $t_n (t_n = n\Delta t, n = 0, \dots, N-1)$  has to be interpolated or upsampled from significantly downsampled the boundary series  $t'_m (t'_m = m\Delta t', m = 0, 1, \dots, M-1)$  using the factor  $r$ , say,  $\Delta t' = r\Delta t, M = N/r$ . The  $m$ th subsampled snapshot is the closest one to the current time level  $n$  in the sense that

$$m = \lfloor n/r \rfloor, \quad (9)$$

where  $\lfloor n/r \rfloor$  indicates the largest integer no greater than  $n/r$ . For brevity, we coin the computation of the Fourier coefficients using DFT as folding (because it folds the time sequence into frequency

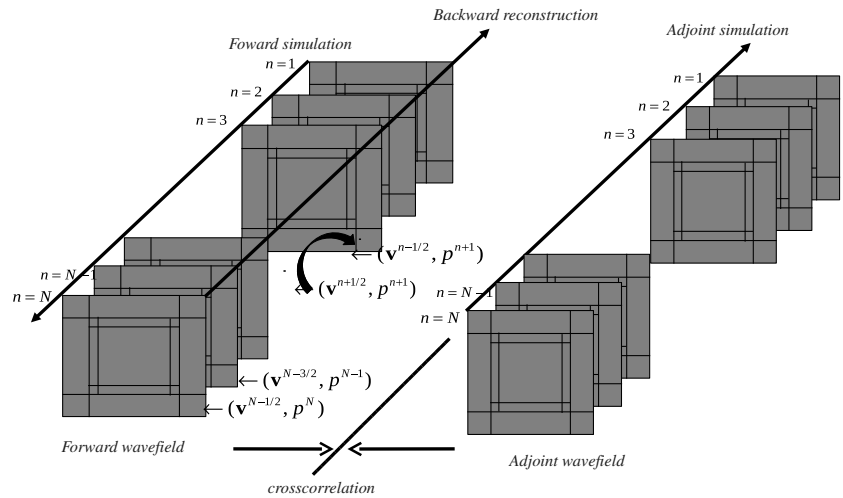


Figure 1. A schematic diagram of wavefield reconstruction for crosscorrelation when applying imaging condition in RTM or building the gradient of the misfit function in FWI in the time domain.

coefficients), and the interpolation of the signal in time as unfolding (because it unfolds the time sequence from the frequency components) hereafter.

- 1) Folding: Applying DFT for the saved boundaries of length  $M$  can then be written as

$$\tilde{u}(\mathbf{x}, k) = \sum_{m=0}^{M-1} u(\mathbf{x}, t'_m) e^{-j\frac{2\pi k}{M}m}, \quad k=0, 1, \dots, M-1, \quad (10)$$

where  $k$  is a frequency index. The process of folding can be done during the forward modeling on the fly at each time step to avoid any saving of the time series.

- 2) Unfolding: Keep in mind that the interpolated wavefield has to be real-valued. According to equations A-5 and A-8 in Appendix A, we restore the wavefield in the boundary storing area  $\Omega_b$  by Fourier interpolation via

$$u(\mathbf{x}, t_n) = \frac{1}{M} \left( \sum_{k=0}^{\frac{M}{2}-1} \tilde{u}(\mathbf{x}, k) e^{j\frac{2\pi kn}{N}} + \sum_{k=\frac{M}{2}}^{M-1} \tilde{u}(\mathbf{x}, k) e^{j\frac{2\pi(k-M)n}{N}} \right) \quad \text{for odd } M \quad (11)$$

or

$$u(\mathbf{x}, t_n) = \frac{1}{M} \left( \sum_{k=0}^{\frac{M}{2}-1} \tilde{u}(\mathbf{x}, k) e^{j\frac{2\pi kn}{N}} + \tilde{u}\left(\mathbf{x}, \frac{M}{2}\right) \cos\left(\frac{\pi n}{r}\right) + \sum_{k=\frac{M}{2}+1}^{M-1} \tilde{u}(\mathbf{x}, k) e^{j\frac{2\pi(k-M)n}{N}} \right) \quad \text{for even } M. \quad (12)$$

The process above is equivalent to applying inverse fast Fourier transform after padding zeros to the sequence  $\tilde{u}(\mathbf{x}, k)$  to be of length  $N$ . Similar to the process of folding, the process of unfolding is done on the fly during the backward reconstruction of the forward wavefield.

The conjugate symmetry of the Fourier spectrum is implied from the real nature of the wavefield:  $u(\mathbf{x}, N-k) = u^*(\mathbf{x}, k)$  in which  $*$  takes the conjugate. As a result, it is not necessary to save all the negative frequencies of the wavefield. The folding is evaluated by

$$\tilde{u}(\mathbf{x}, k) = \sum_{m=0}^{M-1} u(\mathbf{x}, t'_m) e^{-j\frac{2\pi k}{M}m} = \sum_{m=0}^{M-1} u(\mathbf{x}, t_{mr}) e^{-j\frac{2\pi k}{M}m},$$

$$k = 0, 1, \dots, \lfloor M/2 \rfloor + 1, \quad (13)$$

where  $\lfloor M/2 \rfloor$  takes the largest integer no greater than  $M/2$ . With an initialization  $\tilde{u}(\mathbf{x}, k) = 0$ , the implementation of the DFT in each loop over  $t_n$  invokes a multiplication between the wavefield  $u(\mathbf{x}, t_n)$ ,  $\mathbf{x} \in \Omega_b$  and the complex exponential factor  $e^{-j(2\pi k/N)mr}$  if  $t_n$  is the boundary storing time  $t'_m$  ( $t_n = t'_m$ ;  $n = mr$ ):

$$\tilde{u}(\mathbf{x}, k) + = u(\mathbf{x}, t_n) e^{-j\frac{2\pi kn}{N}}, \quad \text{if } n = mr, \quad (14)$$

where  $+ =$  is an accumulation symbol in the sense that  $a+ = b$  is equivalent to  $a = a + b$ . After the whole time stepping, the Fourier coefficients are obtained. Based on the computed positive frequencies, the final expression of the unfolding process reads

$$u(\mathbf{x}, t_n) = \begin{cases} \frac{1}{M} \left( \tilde{u}(\mathbf{x}, 0) + 2\Re \left\{ \sum_{k=1}^{\frac{M}{2}-1} \tilde{u}(\mathbf{x}, k) e^{j\frac{2\pi kn}{N}} \right\} \right) & \text{for odd } M \\ \frac{1}{M} \left( \tilde{u}(\mathbf{x}, 0) + 2\Re \left\{ \sum_{k=1}^{\frac{M}{2}-1} \tilde{u}(\mathbf{x}, k) e^{j\frac{2\pi kn}{N}} \right\} + \tilde{u}\left(\mathbf{x}, \frac{M}{2}\right) \cos\left(\frac{\pi n}{r}\right) \right) & \text{for even } M \end{cases} \quad (15)$$

where  $\Re$  denotes the real part.

### Wavefield reconstruction via Kaiser windowed sinc interpolation

In the context of wavefield reconstruction based on the significantly decimated boundaries, the implementation of DFT/sinc interpolation uses the global Fourier basis as the basis function, implying a heavy computational cost because all the frequency components have to be calculated during the forward simulation, and they have to be used to interpolate the missing/unsampled time levels during the reverse propagation process. In the time domain, the global sinc function has an infinite number of interpolating points in its support. The most intuitive approach to mitigate the computational complexity is to go to local basis function by applying a window on the sinc function. Hence, we propose a Kaiser windowed sinc interpolation algorithm for wavefield reconstruction using the significantly decimated boundaries. The use of Kaiser window makes us easy to tune the window shape and the amplitude spectrum.

Denote  $W$  as the support window describing the index of  $2l$  time levels ( $l$  prior and  $l$  posterior to current time level  $n$ ) and the expression  $a_1 : a_2$  looping over all integers between  $a_1$  and  $a_2$ . We now address the interpolation with special care for the starting and the ending time levels.

- 1) The time levels in the middle if  $m \geq l$  and  $m+l \leq M-1$ , as shown in Figure 2a:  $W = (m-l+1) : (m+l)$ .
- 2) The starting time levels if  $m < l$ , as shown in Figure 2b:  $W = 1 : 2l$ .
- 3) The ending time levels if  $m+l > M-1$ , as shown in Figure 2c:  $W = (M-2l+1) : M$ .

At every time step  $t_n$  the wavefield  $u(\mathbf{x}, t_n)$  in the boundary saving area  $\mathbf{x} \in \Omega_b$  during backward propagation can then be recovered accord-

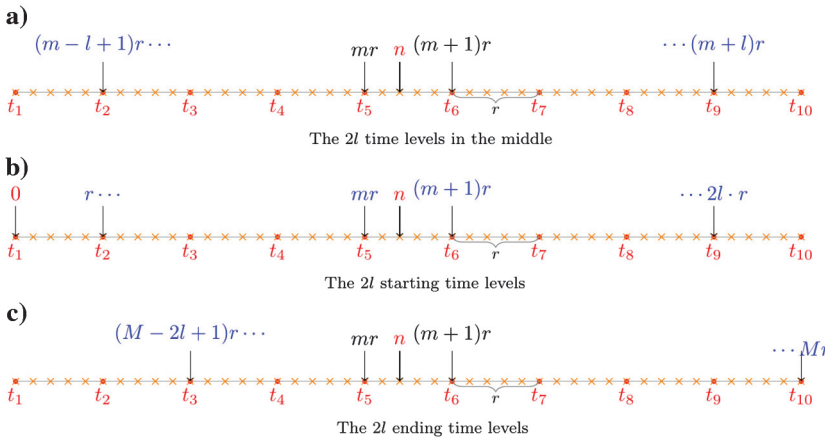


Figure 2. The  $2l$  time levels within the Kaiser window.

ing to the Kaiser windowed sinc interpolation formula in equation B-3

$$u(\mathbf{x}, t_n) = \sum_{i \in W} u(\mathbf{x}, t'_i) w(t_n - t'_i) h(t_n - t'_i). \quad (16)$$

Note that  $t'_i = i\Delta t' = ir\Delta t$  and  $t_n = n\Delta t$ , we have

$$h(t_n - t'_i) = \text{sinc}\left(\frac{n\Delta t - ir\Delta t}{\Delta t'}\right) = \text{sinc}\left(\frac{n - ir}{r}\right) \quad (17)$$

and

$$w(t_n - t'_i) = \begin{cases} \frac{I_0\left(b\sqrt{1-\left(\frac{n-ir}{lr}\right)^2}\right)}{I_0(b)}, & |n - ir| \leq lr \\ 0, & \text{otherwise.} \end{cases} \quad (18)$$

It is important to emphasize that the ending time levels (or the final snapshots) play a role in the initial condition in wavefield reconstruction: The interpolation errors at these time levels may propagate during the whole process of backward reconstruction. Therefore, we do not expect that the interpolation of these time levels becomes extrapolation out of decimating support which is usually unstable. It is also a reason why we carefully handle the starting and ending time levels to reduce the possible interpolation errors during reverse propagation.

### Wavefield reconstruction via Lagrange polynomial interpolation

In the family of local basis interpolation, the classic Lagrange polynomial interpolation also provides us a useful tool to use only local neighboring time levels in boundary interpolation, to mitigate the computation cost of wavefield reconstruction while achieving high interpolation performance with an appropriate order of polynomial. The theoretical result shows that Lagrange interpolation is equivalent to windowed-sinc interpolation using binomial window (Kootsookos and Williamson, 1996).

The interpolation polynomial in Lagrange form is expressed as

$$p(t) = \sum_{i=0}^q y_i \ell_i(t), \quad \ell_i(t) = \prod_{j=0, j \neq i}^q \frac{(t - t_j)}{(t_i - t_j)}, \quad (19)$$

where  $y_i$  is the interpolating points acquired during sampling and  $\ell_i(t)$  is the Lagrange basis function. Let us denote  $n_b$  the number of time levels prior to the current time level  $n$ . A typical value is  $n_b = \lfloor q + 1/2 \rfloor$ . The  $q + 1$  time levels related to the time index  $n$  required by polynomial interpolation are given as follows:

- 1) The time levels in the middle if  $m - (n_b - 1) \geq 1$  and  $m + (q + 1 - n_b) < M$ , as illustrated in Figure 3a:  $W = [m - (n_b - 1)] : [m + (q + 1 - n_b)]$ , where  $W$  includes  $q + 1$  time levels.

- 2) The starting time levels if  $m - (n_b - 1) < 1$ , as shown in Figure 3b:  $W = 1 : (q + 1)$ .
- 3) The ending time levels if  $m + (q + 1 - n_b) \geq M$ , as shown in Figure 3c:  $W = (M - q) : M$ .

At every time step  $t_n$  the wavefield  $u(\mathbf{x}, t_n)$  in the boundary saving area  $\mathbf{x} \in \Omega_b$  during the backward propagation can then be interpolated according to equation 19:

$$u(\mathbf{x}, t_n) = \sum_{i \in W} u(\mathbf{x}, t'_i) \ell_i(t_n). \quad (20)$$

### INTERPOLATION STUDY WITH 1D SYNTHETIC SIGNAL

We now perform a comparative investigation on the accuracy of the three interpolation methods using a realistic synthetic seismic signal. To mimic the true seismic traces within seismic frequency band, we construct an artificial seismic trace by convolution between a Ricker wavelet and a series of reflectivity with non-Gaussian distribution (Walden, 1985; van der Baan and Fomel, 2009):

$$s(t) = r(t) * g(t), \quad (21)$$

where  $*$  stands for the convolution in time. The reflectivity  $g(t)$  is generated from a cubic power of normal distribution with zero mean and unit variance (Claerbout [1992], p. 180). Because the Ricker wavelet  $r(t)$  we used has the peak frequency of  $f_p = 16$  Hz, the maximum frequency can be roughly estimated according to the empirical formula:  $f_{\max} \approx 2.5f_p = 40$  Hz. The temporal sampling interval and the total number of the points are, respectively, set to be  $\Delta t' = 1$  ms and  $N = 1800$ , to mimic the temporal sampling determined by CFL condition and the simulation duration of wave propagation using FD method. The frequency sampling of the signal can be easily computed  $f'_s = 1/\Delta t' = 1000$  Hz. After downsampling the true synthetic signal (Figure 4) with a factor of  $r = 10$ , the resulting signal has its own sampling rate  $f_s = f'_s/r = 100$  Hz, which still satisfies the Nyquist sampling theorem  $f_s \geq 2f_{\max}$ . Based on the decimated version of the raw signal in equation 21, we perform the interpolation with different interpolation methods to evaluate their accuracy. In Lagrange polynomial interpolation, we have to deter-

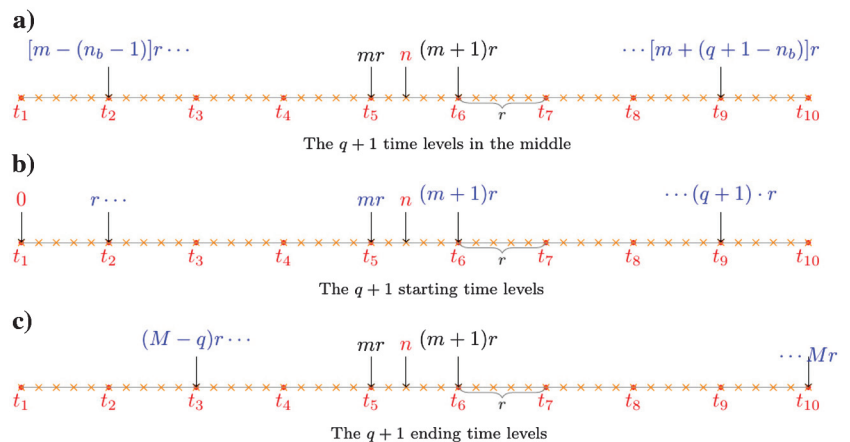


Figure 3. The  $q + 1$  time levels used in the Lagrange polynomial interpolation.



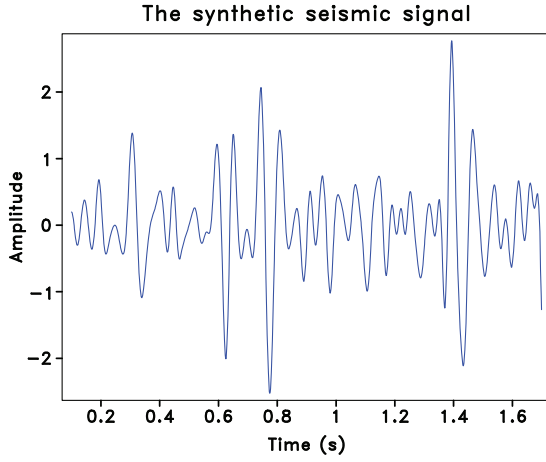


Figure 4. The synthetic seismic trace with  $N = 1800$  points and temporal sampling interval  $\Delta t' = 1$  ms.

**Table 1. Least-squares errors of different interpolation methods.**

Interpolation method	Window length	L2 norm of the error trace
DFT/sinc	$N = 1800$	0.0202687
Kaiser windowed sinc	$2l = 2$	2.33783
	$2l = 4$	0.64739
	$2l = 6$	0.261328
	$2l = 8$	0.172233
	$2l = 10$	0.120056
	$2l = 12$	0.0900108
	$2l = 16$	0.06158
	$2l = 20$	0.0431297
	$2l = 24$	0.404137
	$2l = 28$	0.401023
	$2l = 32$	0.318196
	$2l = 34$	0.350412
	$2l = 36$	0.283237
Lagrange polynomial	$q + 1 = 2$	14.0061
	$q + 1 = 4$	1.76405
	$q + 1 = 6$	0.738518
	$q + 1 = 8$	0.40633
	$q + 1 = 10$	0.256635
	$q + 1 = 12$	0.177903
	$q + 1 = 16$	0.104443
	$q + 1 = 20$	0.0735127
	$q + 1 = 24$	0.0577398
	$q + 1 = 28$	0.047562
	$q + 1 = 32$	0.0522068
	$q + 1 = 34$	0.0777857
	$q + 1 = 36$	0.117725

mine the polynomial order  $q$ , which means  $q + 1$  points are used to interpolate one location. Similarly, in Kaiser windowed sinc interpolation we have to determine the half-length of the Kaiser window  $l$ , which means  $2l$  points are used to interpolate one location. To avoid the misleading effect from the edges, we select the middle part of the signal to compute the errors/differences between the true signal and the interpolated one, and evaluate the least-squares errors by summing over all selected samples in the error trace as well.

Using the setup above, we experimented with several representative window length and ended up with a well understanding of the interpolation performance as shown in Table 1. One of the good results using three different interpolation methods (DFT interpolation, Lagrange polynomial interpolation of seventh order, and Kaiser windowed sinc interpolation with eight-point window) are plotted in Figure 5. The signals are nicely interpolated from a visual perspective. The corresponding errors depicted in Figure 5 are obtained by subtracting the interpolated trace and the true signal in Figure 4. The table and the figure show that the DFT interpolation is the most accurate choice among all methods. The interpolation accuracy of the Lagrange polynomial and Kaiser windowed sinc is low if the number of interpolating points is inadequate. With enough interpolating points, the Lagrange polynomial interpolation and Kaiser windowed sinc interpolation are able to produce accurate result, although the accuracy is not as good as DFT interpolation. Compared with Lagrange interpolation, Kaiser windowed sinc interpolation has a little smaller interpolation error using the same number of interpolating points when the decimating rate  $r$  is high. It is interesting to note that using too many interpolating points does not necessarily lead to higher interpolation accuracy (less interpolation error) for Lagrange polynomial interpolation and Kaiser windowed sinc interpolation: They exhibit Gibbs' phenomenon (or Runge problem in the language of Lagrange interpolation). The numerical experiments show that the window length of eight points is a good trade-off between the computation and accuracy for the Lagrange polynomial interpolation and Kaiser windowed sinc interpolation. That is, seventh-order Lagrange polynomial and eight-point Kaiser window usually yield nice results without significant sacrifice the computation efficiency. In practice, there is no need to go to Gibbs' or Runge problem with a very long window.

## NUMERICAL EXAMPLES

Now we demonstrate the utility of the proposed methods using the Marmousi model. The source is deployed at the center of the models to observe the phenomena of wave propagation going through the whole model. To evaluate the agreement between reconstructed wavefield based on the significantly downsampled boundaries using different interpolation algorithms and the original source wavefield, we introduce the total energy measure

$$E(t) = \frac{1}{2} \int_{\Omega} \left( \rho \mathbf{v}^2(\mathbf{x}, t) + \frac{1}{\kappa} p^2(\mathbf{x}, t) \right) d\mathbf{x}, \quad (22)$$

which is the sum of two parts: One is the kinematic part related to the particle velocity describing the wave motion, and the other is the potential part related to the pressure storing the energy in a spring mechanism. The total energy measures the variations of the wavefield from a macroperspective. A microsurvey of the reconstruction performance can be monitored from a randomly extracted trace. The

window length of the Kaiser-sinc interpolation and the Lagrange interpolation is chosen to be eight points ( $l = 4$ ,  $q = 7$ ) for a good balance of efficiency and interpolation accuracy, according to the previous 1D synthetic study.

In homogeneous medium, the decimating ratio can reach up to five in three dimensions and four in two dimensions. In heterogeneous medium with high velocity contrast, the decimating rate can be much larger than the case of the homogeneous medium. Take the Marmousi model for example. After downsampling the original Marmousi model (Figure 6) with a factor of three in vertical and horizontal axes, we obtain the raw inhomogeneous data of size  $n_z \times n_x = 251 \times 767$  for the test, leading to the grid spacing  $\Delta x = \Delta z = 12$  m. The Ricker wavelet is used again with the peak frequency  $f_m = 10$  Hz. The forward simulation is done for  $N = 3600$  time steps using the temporal sampling  $\Delta t = 0.001$  s. Due to the high velocity contrast of the Marmousi model ( $v_{\min} = 1500$  m/s,  $v_{\max} = 5500$  m/s), we first test wavefield reconstruction with DFT interpolation using a much larger downsampling ratio  $r = 15$  while monitoring the two snapshots at time  $n = 400$  and  $1200$ , as shown in Figure 7a–7d. The experiment is then repeated using seventh-order Lagrange polynomial and eight-point Kaiser windowed sinc interpolation. As shown in Figure 7e–7h, the reconstructed wavefields using Kaiser windowed sinc interpolation and Lagrange polynomial interpolation for the boundary are also satisfactory because the amplitudes of the error panels are less than two orders of magnitude of the forward simulated wavefield in Figure 7a and 7b. The energy curves in Figure 8a–8c are essentially indistinguishable due to excellent reconstruction (and small errors in Figure 8d–8f) of the proposed methods. It is also interesting to find that

in this example DFT method outperforms the other two methods, according to the least-squares errors in Table 2.

The accurate reconstruction has been confirmed based on the energy measure in the whole domain. A further intuitive justification is monitoring a seismic trace recorded at a specific location in the model. We extract a trace at the grid point (100, 100) to further evaluate the wavefield reconstruction performance using different boundary interpolation techniques. The results obtained from DFT-based reconstruction, Kaiser sinc interpolation-based reconstruction (with eight-point window) and the Lagrange polynomial-based

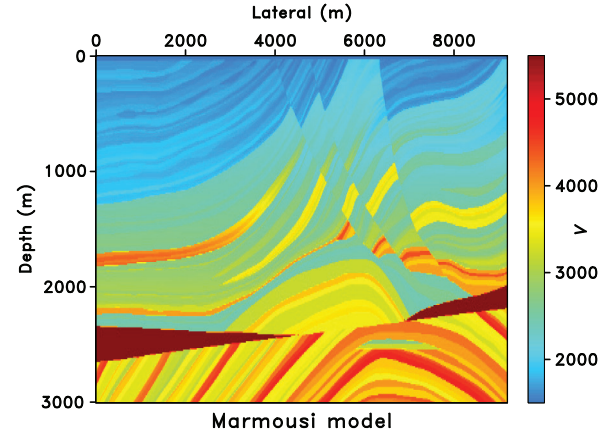


Figure 6. The Marmousi velocity model.

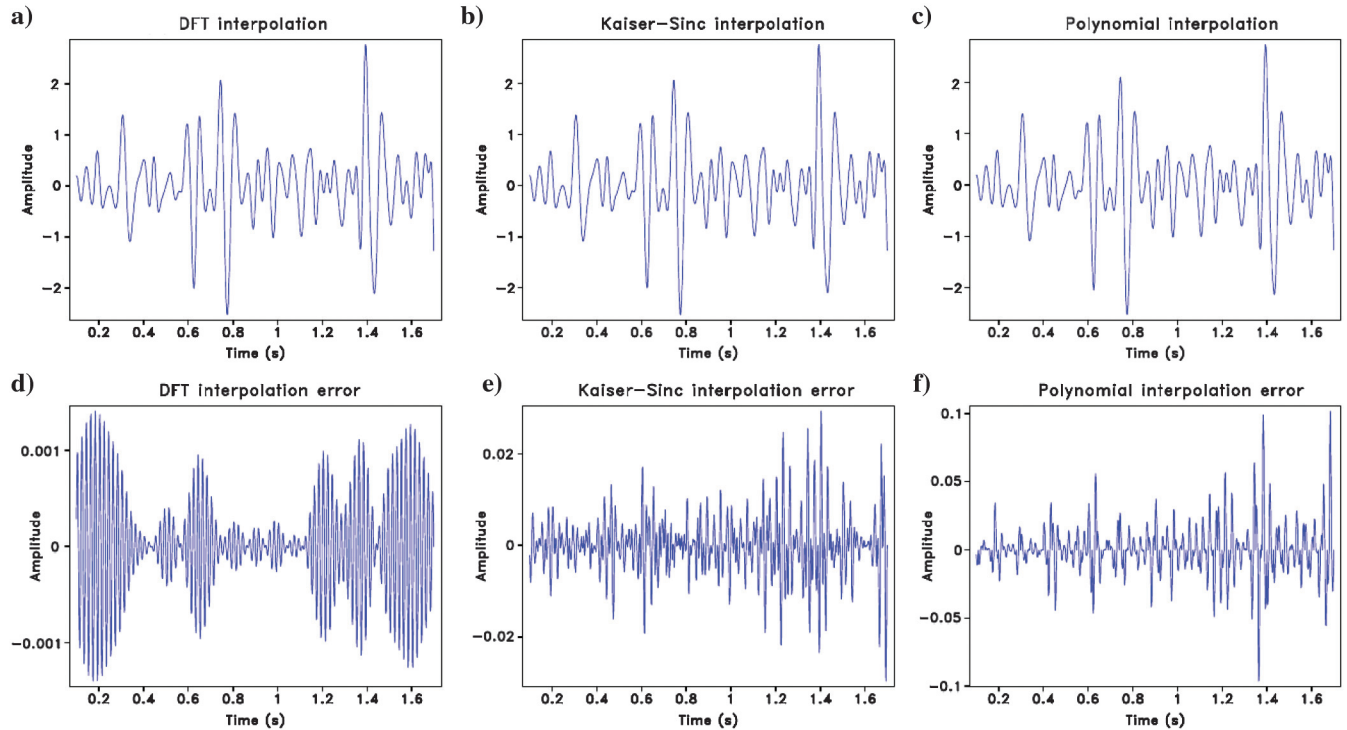


Figure 5. The interpolated seismic traces using (a) DFT interpolation, (b) Lagrange polynomial interpolation, (c) Kaiser windowed sinc interpolation, and (d–f) the associated interpolating errors. All the interpolation methods are able to produce visually nice result. The magnitude of the error trace indicates that DFT interpolation is the most accurate one, while Kaiser windowed sinc interpolation slightly outperforms the Lagrange polynomial algorithm.

reconstruction (with polynomial of order seven) are shown in Figure 9a–9c, respectively. As can be seen from Figure 9d–9f, the errors between the forward simulated trace and backward reconstructed trace are quite small. We again observed that Kaiser-sinc interpolation and Lagrange polynomial interpolation produces similar accurate results, even though the error of Lagrange polynomial interpolation method is slightly larger than the error of Kaiser-sinc

interpolation method, however, still remaining at the same magnitude level.

## DISCUSSION ON COMPUTATION AND STORAGE IN THREE DIMENSIONS

After the numerical demonstration, we perform a comparative study on the storage and computation complexity for the wavefield reconstruction techniques based on DFT interpolation, Kaiser windowed sinc interpolation and Lagrange polynomial interpolation, to show the pros and cons for both methods proposed above.

Let us consider a 3D model of size  $nx \times ny \times nz$ . Allowing for minimum boundary saving burden using  $2J$ th order staggered grid FD modeling for  $N$  time steps,  $2J - 1$  layers for saving single state variable  $\mathbf{v}/p$  (Yang et al., 2014a, 2014b; Nguyen and McMechan, 2015) or  $2J$  layers for saving double state variables  $(\mathbf{v}, p)$  on each face (left and right, top and bottom, front and rear) of the cube are required for perfect reconstruction of the wavefield. The total number of gridpoints required at each time step by storing single state variable  $\mathbf{v}$  is given by

$$S = 2(2J - 1)(nx \times ny + nx \times nz + ny \times nz). \quad (23)$$

Assuming single precision (one real value needs 4 bytes) in the computation of wave propagation, the original time-domain wavefield reconstruction scheme needs

$$NS \times 4 \text{ (bytes)} \quad (24)$$

memory consumption without any computational efforts because the saved boundaries are directly stuffed in their corresponding locations in backward reconstruction. The proposed DFT interpolation algorithm for wavefield reconstruction with a downsampling factor  $r$  involves

$$\frac{N}{r} \times S \times \frac{1}{2} \times 8 \text{ (bytes)} \quad (25)$$

to store the Fourier coefficients (one complex-valued coefficient needs 8 bytes while only positive frequencies are saved) of the boundary elements during folding procedure which are computed with following amount of flops  $(N/r)^2 \times S$ , while further floating point operations are still necessary in the unfolding from the Fourier coefficients to the interpolated time domain signals:  $(N^2/r) \times S$ .

Let us now consider a realistic 3D computing volume modeling 4000 time steps using fourth-order staggered grid FD:  $nx = ny = nz = 300$ ,  $N = 4000$ , and  $2J = 4$ . Assume single state variable saving. The wavefield reconstruction scheme using boundaries saved at every time step leads to the following memory requirement:

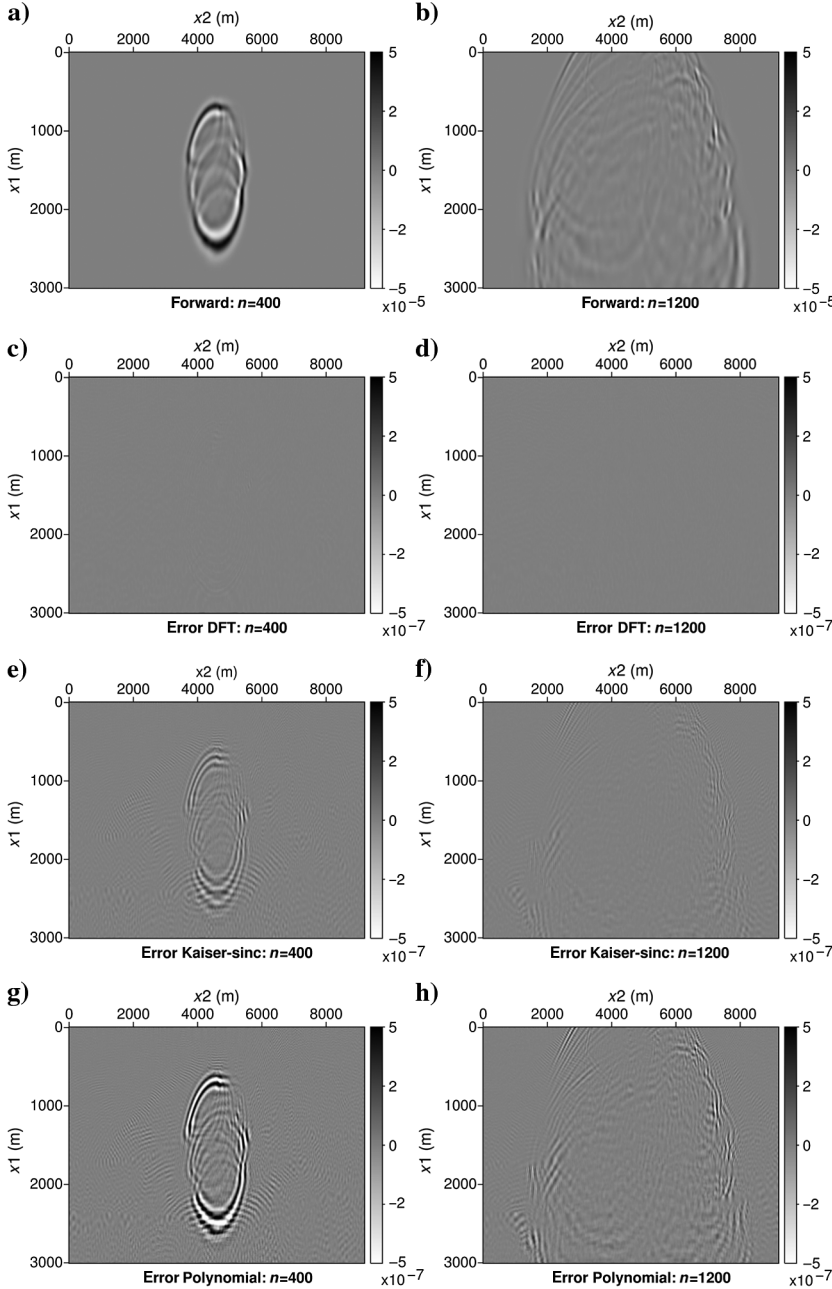


Figure 7. (a and b) With the downsampling rate  $r = 15$ , two snapshots are recorded during forward modeling in Marmousi model. Good reconstruction performance is demonstrated using (c and d) DFT-based boundary interpolation and excellent reconstruction performance using (e and f) Kaiser windowed sinc interpolation and (g and h) Lagrange polynomial interpolation. Note that the amplitude of the error panels in (b-d) are two to three orders of magnitude smaller compared with the forward simulated wavefield in (a and b).



$$N \times S \times 4/1024^3 = 4000 \times 2 \times 3 \times 3 \times 300^2 \\ \times 4/1024^3 = 24.14 \text{ (GB)}, \quad (26)$$

which makes in-core boundary saving difficult in many state-of-the-art machines. For a realistic acoustic model  $v_{\max}/v_{\min} \geq 2$ , the down-sampling factor will be greater than 10, namely,  $r > 10$ . Thus, the memory consumption for the proposed method needs

$$24.14/r < 2.42 \text{ (GB)} \quad \text{for 3D acoustic media.} \quad (27)$$

In elastic media, the velocity contrast would be much higher: the fastest P-wave would be up to 10 times of the slowest S-wave, i.e.,  $v_{\max}/v_{\min} > 10$ . It leads to a decimation rate easily going to 50,  $r > 50$  and the memory consumption can be further reduced to

$$24.14/r < 0.48 \text{ (GB)} \quad \text{for 3D elastic media} \quad (28)$$

which is two orders of magnitude reduction in the sense that the proposed methods are valuable when the velocity model becomes more sophisticated with high velocity contrast. Therefore, the proposed DFT interpolation method enables 3D in-core memory saving for wavefield reconstruction using the Fourier coefficients of the boundaries, at the price of further computational efforts when performing the DFT in the simulation on the fly.

The most remarkable advantage of Kaiser windowed sinc interpolation and Lagrange polynomial interpolation algorithm over the DFT interpolation algorithm is the low computational complexity. Instead of computing and storing all positive frequencies, the bound-

ary saving remains in time domain during the forward simulation. During backward reconstruction, the unsampled boundary elements are computed according to its local neighboring time levels. For each spatial point in the boundary saving area, the total number of floating point operations required by the DFT interpolation is of order  $O(N^2)$ , while the flops of the other two methods are of order  $O(N)$ , which is extremely small compared with the DFT method. The total number of flops is obtained by multiplying a factor of  $S$  in equation 23. The memory consumption for wavefield reconstruction via Lagrange polynomial interpolation and Kaiser windowed sinc interpolation is close to the DFT interpolation method. The memory consumption may still highly increase when very high order of FD scheme is used to reduce the numerical dispersion. By using the technique proposed by Hu (2014), one may still use fourth-order FD while maintaining numerical dispersion smaller than conventional 16th order FD. Therefore, the boundary storage issue could still be mitigated a lot.

**Table 2. Least-squares errors of wavefield snapshots at different time: Marmousi model.**

Method	$n = 400$	$n = 1200$
DFT/sinc	4.93646e-06	4.52236e-06
Kaiser windowed sinc	1.43757e-05	7.4763e-06
Lagrange polynomial	3.70816e-05	1.85111e-05

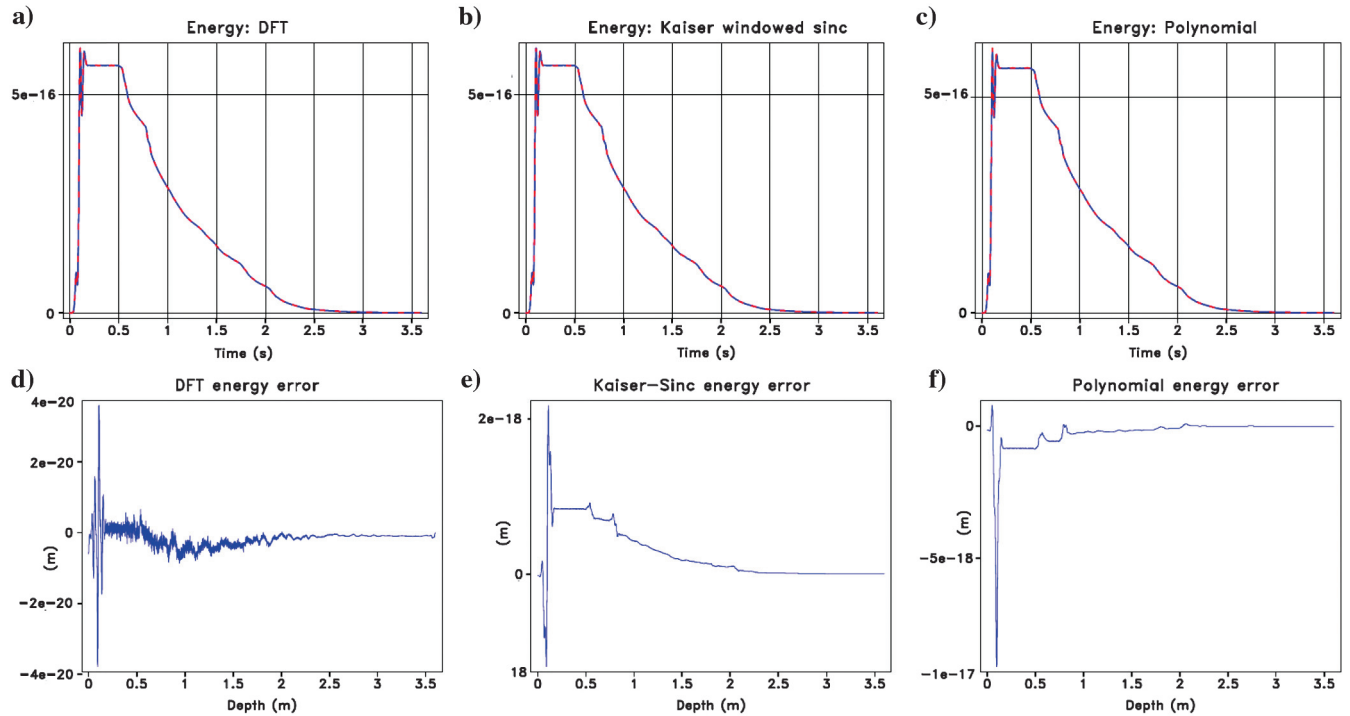


Figure 8. (a-c) The energy curve in the backward propagation using the three methods exactly matches their counterpart in the forward simulation. (solid: forward; dashed: backward) The errors are so small that the differences between solid and dashed line in (a-c) are indistinguishable. (d-f) By subtracting the two lines, the errors are displayed with at least two orders of magnitude smaller compared with the true values of the energy.

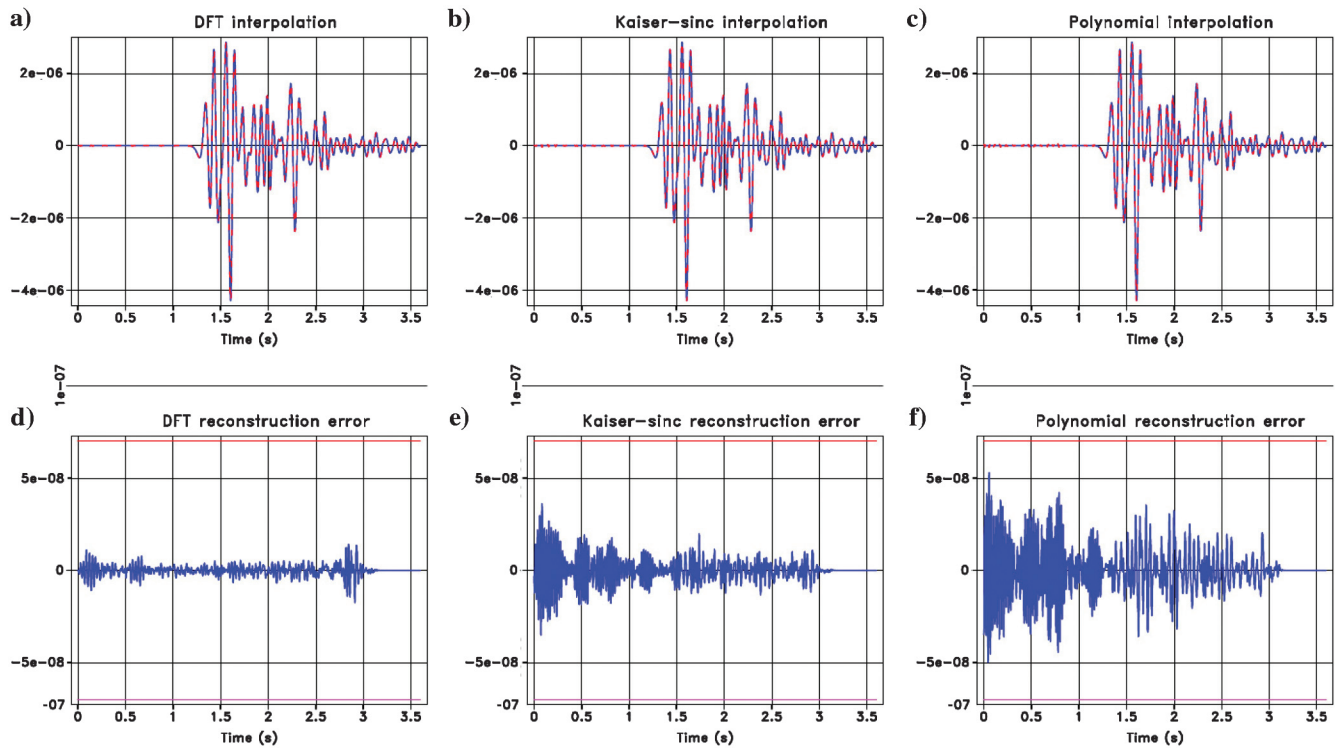


Figure 9. Trace comparison of wavefield reconstruction methods for the Marmousi model at location (100, 100). Top line (a-c): In each panel, the interpolated signals (solid) exactly match the raw trace (dash) using different method; bottom line (d-f): The corresponding error traces obtained by subtracting the interpolated signal with the true one. Note that the amplitude of the errors is several order of magnitude smaller than the original signal.

## CONCLUSIONS

In this paper, we have implemented three algorithms, such as the DFT/sinc interpolation method, the Kaiser windowed sinc interpolation, and the Lagrange polynomial interpolation method, to carry out wavefield reconstruction by interpolating the significantly decimated boundaries. The DFT/sinc interpolation uses global Fourier basis as the interpolating basis, whereas the other two methods use the local basis functions, such as the Kaiser windowed sinc function and the Lagrange polynomial within a specific window. From another perspective, these methods are based on three different digital filters. The interpolation errors are caused by the nonflat frequency response of the designed filter. DFT method is equivalent to an IIR filter with a flat spectrum, which is an ideal filter for bandlimited signals while asking for periodicity of the signal; Kaiser window method and the Lagrange interpolation method here are equivalent to FIR filtering using different window functions. Due to the different length of window size for information collocation, the wavefield reconstruction via DFT interpolation technique has excellent accuracy while requesting more computation. Compared with the DFT interpolation method, the wavefield reconstruction using Kaiser windowed sinc interpolation and Lagrange polynomial interpolation are much more efficient without significant sacrifice of wavefield reconstruction quality. A careful reminder is that the DFT-based method suffers from the periodicity condition. The violation of periodicity may slightly deteriorate its performance sometimes, although it is theoretically sound. The limitation for Kaiser win-

dowed sinc interpolation and Lagrange interpolation is that they suffer from Gibbs' phenomenon or Runge problem: Using too high order of an interpolating polynomial does not necessarily lead to higher interpolation accuracy.

These methods have the potential to reduce the boundary saving burden at least one order of magnitude in acoustic media and two orders of magnitude in elastic media, therefore enabling efficient computation of 3D imaging problems (such as RTM and FWI) of moderate size using the boundary saving in core. The implementation has been carried out for 2D case and the first-order wave equation system, and can be applied to 3D and second-order wave equation system straightforwardly. Other interpolating techniques such as cubic splines involving heavy memory consumption for storing a triangular matrix ( $n$ -point unknown interpolating weight vector lead to  $3n - 2$  nonzero elements of the triangular matrix) are out of the scope of this paper. Once the wave imaging problem becomes extremely large, storing on disk may still be useful compensated by the techniques described in the paper. The data compression techniques may also be combined to further stave off the growing overhead of the memory storage when addressing 3D imaging problems.

## ACKNOWLEDGMENTS

We thank S. Operto, L. Métivier, and S. Fomel for inspiring discussions. We appreciate the valuable comments and additions from J. Etgen, S. Hestholm, P. Moghaddam, and three anonymous reviewers.

This study was partially funded by the SEISCOPE consortium (<http://seiscope2.osug.fr>), sponsored by BP, CGG, CHEVRON, EXXON-MOBIL, JGI, PETROBRAS, SAUDI ARAMCO, SCHLUMBERGER, SHELL, SINOPEC, STATOIL, TOTAL, and WOODSIDE. This study was granted access to the HPC resources of the Froggy platform of the CIMENT infrastructure (<https://ciment.ujf-grenoble.fr>), which is supported by the Rhône-Alpes region (GRANT CPER07\_13 CIRA), the OSUG@2020 labex (reference ANR10 LABX56), and the Equip@Meso project (reference ANR-10-EQPX-29-01) of the programme Investissements d'Avenir supervised by the Agence Nationale pour la Recherche, and the HPC resources of CINES/IDRIS under the allocation 046091 made by GENCI.

## APPENDIX A

### FOURIER INTERPOLATION OF REAL-VALUED SIGNALS

Based on the theory of Fourier series, all the signal can be expanded as many sinusoids with different frequencies. By enforcing periodicity with equal-space discretization, a continuous signal with a finite duration of length  $T = M\Delta t'$  is the combination of Fourier series which can be computed via

$$\begin{aligned} s(\omega_k) &= \int_0^T s(t) e^{-j\omega_k t} dt, \omega_k = \frac{2\pi k}{T} = \frac{2\pi k}{M\Delta t'} \\ &= \Delta t' \sum_{m=0}^{M-1} s(m\Delta t') e^{-j\frac{2\pi km}{M}} \\ &\quad (t = m\Delta t', k = 0, 1, \dots, M-1). \end{aligned} \quad (\text{A-1})$$

Neglecting the constant  $\Delta t'$  with the notation  $s(m\Delta t') := s_m$ ,  $\tilde{s}(\omega_k) = \tilde{s}_k$ , we have the DFT

$$\tilde{s}_k = \sum_{m=0}^{M-1} s_m e^{-j\frac{2\pi km}{M}} \quad (k = 0, 1, \dots, M-1) \quad (\text{A-2})$$

and the signal is then reconstructed via the inverse DFT

$$s_m = \frac{1}{M} \sum_{n=0}^{M-1} \tilde{s}_k e^{j\frac{2\pi km}{M}} \quad (k = 0, 1, \dots, M-1). \quad (\text{A-3})$$

The time and frequency scaling properties of the Fourier transform inspire us to construct a new signal  $h_n$  of length  $N = rM$  which can reduce to  $s_m$  after downsampling with a factor  $r$ . It is done by zero-stuffing the frequency spectrum of  $s_m$ . To ensure the interpolated  $h_n$  time sequence is real only, the conjugate symmetry must be maintained in the zero-stuffed frequency samples  $\tilde{h}_k = \tilde{h}_{N-k}$ . Due to the real signal  $s_m$ , the conjugate symmetry  $\tilde{s}_k = \tilde{s}_{M-k}^*$  has been well-satisfied before inserting zeros. This spectrum symmetry should also be maintained to guarantee that the DFT-interpolated signal is still real valued. When  $M$  is an odd number, we construct the Fourier coefficients of  $h_n$  in the following:

$$\tilde{h}_k = \begin{cases} r\tilde{s}_k, & k = 0, \dots, \frac{M-1}{2} \\ r\tilde{s}_{k-(r-1)M}, & k = (rM - \frac{M+1}{2}), \dots, rM-1 \\ 0, & \text{otherwise} \end{cases} \quad (\text{A-4})$$

the signal  $h_n$  in the time domain is then obtained by inverse DFT

$$\begin{aligned} h_n &= \frac{1}{N} \sum_{k=0}^{N-1} \tilde{h}_k e^{j\frac{2\pi kn}{N}} \\ &= \frac{1}{rM} \left( \sum_{k=0}^{\frac{M-1}{2}} r\tilde{s}_k e^{j\frac{2\pi kn}{rM}} + \sum_{k=rM-\frac{M+1}{2}}^{rM-1} r\tilde{s}_{k-(r-1)M} e^{j\frac{2\pi kn}{rM}} \right) \\ &= \frac{1}{M} \left( \sum_{k=0}^{\frac{M-1}{2}} \tilde{s}_k e^{j\frac{2\pi kn}{rM}} + \sum_{k=\frac{M+1}{2}}^{M-1} \tilde{s}_k e^{j\frac{2\pi(k+(r-1)M)n}{rM}} \right) \\ &= \frac{1}{M} \left( \sum_{k=0}^{\frac{M-1}{2}} \tilde{s}_k e^{j\frac{2\pi kn}{rM}} + \sum_{k=\frac{M+1}{2}}^{M-1} \tilde{s}_k e^{j\frac{2\pi(k-M)n}{rM}} \right) \\ &= \frac{1}{M} \left( \sum_{k=0}^{\frac{M-1}{2}} \tilde{s}_k e^{j\frac{2\pi kn}{rM}} + e^{-j\frac{2\pi n}{r}} \sum_{k=\frac{M+1}{2}}^{M-1} \tilde{s}_k e^{j\frac{2\pi kn}{rM}} \right) \end{aligned} \quad (\text{A-5})$$

where the periodicity of the signal is tacitly used. The signal  $s_m$  can therefore be considered as the downsampled version of  $h_n$  with a factor of  $r$  because

$$\begin{aligned} h_{rm} &= \frac{1}{M} \left( \sum_{k=0}^{\frac{M-1}{2}} \tilde{s}_k e^{j\frac{2\pi krm}{rM}} + e^{-j\frac{2\pi rm}{r}} \sum_{k=\frac{M+1}{2}}^{M-1} \tilde{s}_k e^{j\frac{2\pi krm}{rM}} \right) \\ &= \frac{1}{M} \sum_{k=0}^{M-1} \tilde{s}_k e^{j\frac{2\pi km}{M}} = s_m. \end{aligned} \quad (\text{A-6})$$

To obtain  $h_n$  one may first stuff zeros in the Fourier spectrum to be of length  $rM$ , then perform inverse DFT and multiply  $r$ . Thus, the values of  $h_n$  for  $n \neq rm$  can also be interpolated. This process is the so-called Fourier interpolation.

Special attention has to be paid to the Nyquist frequency  $\tilde{s}_{M/2}$  when  $M$  is an even number. The Fourier spectrum is given by ( $\tilde{s}_{M/2}$  is real because  $\tilde{s}_{M/2} = \sum_{m=0}^{M-1} s_m e^{-j\frac{2\pi M}{2}m} = \sum_{m=0}^{M-1} (-1)^m s_m$ )

$$\tilde{h}_k = \begin{cases} r\tilde{s}_k, & k = 0, \dots, \frac{M}{2}-1 \\ \frac{r}{2}\tilde{s}_{\frac{M}{2}}, & k = \frac{M}{2} \\ \frac{r}{2}\tilde{s}_{\frac{M}{2}}, & k = (r-\frac{1}{2})M \\ r\tilde{s}_{k-(r-1)M}, & k = (r-\frac{1}{2})M+1, \dots, rM-1 \\ 0, & \text{otherwise.} \end{cases} \quad (\text{A-7})$$

The function  $h_n$  is therefore

$$\begin{aligned}
 h_n &= \frac{1}{N} \sum_{k=0}^{N-1} \tilde{h}_k e^{j \frac{2\pi k n}{N}} \\
 &= \frac{1}{rM} \left( \sum_{k=0}^{M-1} r \tilde{s}_k e^{j \frac{2\pi k n}{rM}} + \frac{r}{2} \tilde{s}_{\frac{M}{2}} e^{j \frac{2\pi \frac{M}{2} n}{rM}} + \frac{r}{2} \tilde{s}_{\frac{M}{2}} e^{j \frac{2\pi (r-\frac{1}{2}) M n}{rM}} + \sum_{k=(r-\frac{1}{2})M+1}^{rM-1} r \tilde{s}_{k-(r-1)M} e^{j \frac{2\pi k n}{rM}} \right) \\
 &= \frac{1}{M} \left( \sum_{k=0}^{M-1} \tilde{s}_k e^{j \frac{2\pi k n}{rM}} + \frac{1}{2} \tilde{s}_{\frac{M}{2}} e^{j \frac{2\pi \frac{M}{2} n}{rM}} + \frac{1}{2} \tilde{s}_{\frac{M}{2}} e^{j \frac{2\pi (r-\frac{1}{2}) M n}{rM}} + \sum_{k=\frac{M}{2}+1}^{M-1} \tilde{s}_k e^{j \frac{2\pi (k+(r-1)M) n}{rM}} \right) \\
 &= \frac{1}{M} \left( \sum_{k=0}^{\frac{M}{2}-1} \tilde{s}_k e^{j \frac{2\pi k n}{rM}} + \frac{1}{2} \tilde{s}_{\frac{M}{2}} e^{j \frac{2\pi \frac{M}{2} n}{rM}} + \frac{1}{2} \tilde{s}_{\frac{M}{2}} e^{-j \frac{2\pi \frac{1}{2} M n}{rM}} + \sum_{k=\frac{M}{2}+1}^{M-1} \tilde{s}_k e^{j \frac{2\pi (k-M) n}{rM}} \right) \\
 &= \frac{1}{M} \left( \sum_{k=0}^{\frac{M}{2}-1} \tilde{s}_k e^{j \frac{2\pi k n}{rM}} + \tilde{s}_{\frac{M}{2}} \cos\left(\frac{2\pi \frac{M}{2} n}{rM}\right) + e^{-j \frac{2\pi n}{r}} \sum_{k=\frac{M}{2}+1}^{M-1} \tilde{s}_k e^{j \frac{2\pi k n}{rM}} \right) \\
 &= \frac{1}{M} \left( \sum_{k=0}^{\frac{M}{2}-1} \tilde{s}_k e^{j \frac{2\pi k n}{rM}} + \tilde{s}_{\frac{M}{2}} \cos\left(\frac{\pi n}{r}\right) + e^{-j \frac{2\pi n}{r}} \sum_{k=\frac{M}{2}+1}^{M-1} \tilde{s}_k e^{j \frac{2\pi k n}{rM}} \right) \quad (\text{A-8})
 \end{aligned}$$

It is easy to validate that when  $n = rm$ ,

$$\begin{aligned}
 h_{rm} &= \frac{1}{M} \left( \sum_{k=0}^{\frac{M}{2}-1} \tilde{s}_k e^{j \frac{2\pi k m}{M}} + \tilde{s}_{\frac{M}{2}} (-1)^m + e^{-j \frac{2\pi m}{r}} \sum_{k=\frac{M}{2}+1}^{M-1} \tilde{s}_k e^{j \frac{2\pi k m}{M}} \right) \\
 &= \frac{1}{M} \sum_{k=0}^{M-1} \tilde{s}_k e^{j \frac{2\pi k m}{M}} = s_m. \quad (\text{A-9})
 \end{aligned}$$

Even though excellent efficiency exists in the fast implementation, storing all the boundary elements and performing fast Fourier transform with all saved boundaries at one time to do Fourier interpolation is unaffordable in real applications to FWI due to the large memory consumption. Therefore, turning to DFT with wave propagation on the fly is a judicious approach for practical implementation.

## APPENDIX B

### SINC INTERPOLATION WITH A KAISER WINDOW

As a matter of fact, frequency-domain zero padding is the application of a boxcar on the frequency spectrum of the signal, which is equivalent to time-domain sinc interpolation with infinite number of samples according to Shannon's sampling theorem. For any band-limited signal  $s(t)$  with sampling rate  $\Delta t'$  ( $f_s = (1/\Delta t') \geq 2f_{\max}$ ), the well-known Shannon's sampling theorem guarantees that  $s(t)$  can be uniquely reconstructed from the samples  $s(m\Delta t')$  via

$$s(t) = \sum_{m=-\infty}^{\infty} s(m\Delta t') h(t - m\Delta t'), \quad h(t) = \text{sinc}\left(\frac{t}{\Delta t'}\right), \quad (\text{B-1})$$

where  $h(t)$  is the so-called sinc function. Equation B-1 is a discrete convolution between the signal samples and the sinc function, indicating that the continuous signal can be interpreted as a superposition of each signal samples weighted by shifted and scaled sinc functions. The frequency response of the sinc function  $h(t)$  is a boxcar window

$$\tilde{h}(\omega) = \begin{cases} 1, & |\omega| < \frac{\omega_s}{2} = \frac{\pi}{\Delta t'} \\ 0, & \text{otherwise} \end{cases}. \quad (\text{B-2})$$

Therefore, time-domain sinc interpolation with infinite number of samples is equivalent to frequency-domain windowing with a boxcar: Sinc interpolation picks those intermediate points to be consistent with the Fourier spectrum selected by boxcars (i.e., idealized low-pass or band-pass filters). Sinc interpolation necessarily involves a circular convolution, which is not a finite computation in the time domain. Using DFT is therefore the only practical way to do a sinc interpolation (or circular convolution in general) with a finite number of data points. The application of the boxcar windowing is to keep the low frequency all the same while padding zeros to the frequencies which are higher than Nyquist frequency. The time-domain signal is finally obtained by applying inverse Fourier transform to the zero-padded frequency series.

It is easy to see that computing the infinite support of the global basis in the time domain is impractical. An intuitive approach is to go to local basis by truncating the sinc function using a window function  $w(t)$  with finite support, leading to the following interpolated signal:

$$s(t) := \sum_{m \in W} s(m\Delta t') w(t - m\Delta t') h(t - m\Delta t'), \quad (\text{B-3})$$

where  $W$  is the support of the window  $w(t)$ . The simplest window function is the boxcar, however, sometimes exhibiting severe ringing effect, i.e., the so-called Gibbs' phenomenon. There are many possible candidates available, such as Chebyshev window, Hanning window, and Hamming window et al. The Kaiser window is a simple yet flexible windowing technique for sinc interpolation due to its single tuning parameter  $b$  (Hicks, 2002):

$$w(t) = \begin{cases} \frac{I_0\left(b\sqrt{1-\left(\frac{t}{L}\right)^2}\right)}{I_0(b)}, & |t| \leq L \\ 0, & \text{otherwise} \end{cases}, \quad (\text{B-4})$$

where  $L = l\Delta t'$  is the half-length of the window and  $I_0$  is the modified Bessel function of the first kind of order zero.

## REFERENCES

- Anderson, J. E., L. Tan, and D. Wang, 2012, Time-reversal checkpointing methods for RTM and FWI, *Geophysics*, **77**, no. 4, S93–S103.
- Brossier, R., B. Pajot, L. Combe, S. Operto, L. Métivier, and J. Virieux, 2014, Time and frequency-domain FWI implementations based on time solver: Analysis of computational complexities: 76th Annual International Conference and Exhibition, EAGE, Extended Abstracts, G102 05.
- Claerbout, J. F., 1992, *Earth sounding analysis*: Blackwell Scientific Publications.
- Clapp, R., 2008, Reverse time migration: Saving the boundaries: Technical Report SEP-136, Stanford Exploration Project.
- Clapp, R. G., 2015, Seismic processing and the computer revolution(s): 85th Annual International Meeting, SEG, Expanded Abstracts, 4832–4837.
- Clapp, R. G., 2009, Reverse time migration with random boundaries: 79th Annual International Meeting, SEG, Expanded Abstracts, 2809–2813.
- Dussaud, E., W. W. Symes, P. Williamson, L. Lemaistre, P. Singer, B. Denel, and A. Cherrett, 2008, Computational strategies for reverse-time migration: 78th Annual International Meeting, SEG, Expanded Abstracts, 2267–2271.
- Fomel, S., 2001, Three-dimensional seismic data regularization: Ph.D. thesis, Stanford University.
- Fornberg, B., 1988, Generation of finite difference formulas on arbitrarily spaced grids: *Mathematics of Computation*, **51**, 699–699, doi: [10.1090/S0025-5718-1988-0935077-0](https://doi.org/10.1090/S0025-5718-1988-0935077-0).



- Griewank, A., 1992, Achieving logarithmic growth of temporal and spatial complexity in reverse automatic differentiation: *Optimization Methods and Software*, **1**, 35–54, doi: [10.1080/10556789208805505](https://doi.org/10.1080/10556789208805505).
- Griewank, A., and A. Walther, 2000, Algorithm 799: Revolve: An implementation of checkpointing for the reverse or adjoint mode of computational differentiation: *ACM Transactions on Mathematical Software (TOMS)*, **26**, 19–45, doi: [10.1145/347837.347846](https://doi.org/10.1145/347837.347846).
- Hicks, G. J., 2002, Arbitrary source and receiver positioning in finite-difference schemes using Kaiser windowed sinc functions: *Geophysics*, **67**, 156–165, doi: [10.1190/1.1451454](https://doi.org/10.1190/1.1451454).
- Hu, W., 2014, A nearly exact seismic modeling algorithm for frequency domain FWI: 84th Annual International Meeting, SEG, Expanded Abstracts, 3460–3464.
- Kootsookos, P. J., and R. C. Williamson, 1996, Fir approximation of fractional sample delay systems: *IEEE Transactions on Circuits and Systems II: Analog and Digital Signal Processing*, **43**, 269–271, doi: [10.1109/82.486473](https://doi.org/10.1109/82.486473).
- Nguyen, B. D., and G. A. McMechan, 2015, Five ways to avoid storing source wavefield snapshots in 2D elastic prestack reverse time migration: *Geophysics*, **80**, no. 1, S1–S18, doi: [10.1190/geo2014-0014.1](https://doi.org/10.1190/geo2014-0014.1).
- Shen, X., and R. G. Clapp, 2015, Random boundary condition for memory-efficient waveform inversion gradient computation: *Geophysics*, **80**, no. 6, R351–R359, doi: [10.1190/geo2014-0542.1](https://doi.org/10.1190/geo2014-0542.1).
- Sirgue, L., J. Etgen, and U. Albertin, 2007, 3D full-waveform inversion: Wide versus narrow-azimuth acquisitions: 77th Annual International Meeting, SEG, Expanded Abstracts, 1760–1764.
- Symes, W. W., 2007, Reverse time migration with optimal checkpointing: *Geophysics*, **72**, no. 5, SM213–SM221, doi: [10.1190/1.2742686](https://doi.org/10.1190/1.2742686).
- van der Baan, M., and S. Fomel, 2009, Nonstationary phase estimation using regularized local kurtosis maximization: *Geophysics*, **74**, no. 6, A75–A80, doi: [10.1190/1.3213533](https://doi.org/10.1190/1.3213533).
- Virieux, J., 1986, P-SV wave propagation in heterogeneous media: Velocity-stress finite difference method: *Geophysics*, **51**, 889–901, doi: [10.1190/1.1442147](https://doi.org/10.1190/1.1442147).
- Virieux, J., and S. Operto, 2009, An overview of full waveform inversion in exploration geophysics: *Geophysics*, **74**, no. 6, WCC1–WCC26, doi: [10.1190/1.3238367](https://doi.org/10.1190/1.3238367).
- Walden, A. T., 1985, Non-gaussian reflectivity, entropy, and deconvolution: *Geophysics*, **50**, 2862–2888, doi: [10.1190/1.1441905](https://doi.org/10.1190/1.1441905).
- Yang, P., J. Gao, and B. Wang, 2014a, RTM using effective boundary saving: A staggered grid GPU implementation: *Computers & Geosciences*, **68**, 64–72, doi: [10.1016/j.cageo.2014.04.004](https://doi.org/10.1016/j.cageo.2014.04.004).
- Yang, P., B. Wang, and J. Gao, 2014b, Using the effective boundary saving strategy in GPU-based RTM programming: 84th Annual International Meeting, SEG, Expanded Abstracts, 4014–4021.